

# Nanometer-scale mechanical imaging of aluminum damascene interconnect structures in a low-dielectric-constant polymer

R. E. Geer<sup>a)</sup>

*University at Albany Institute for Materials, State University of New York, Albany, New York 12203*

O. V. Kolosov<sup>b)</sup> and G. A. D. Briggs

*Department of Materials, Oxford University, OX1 3PH, United Kingdom*

G. S. Shekhawat

*University at Albany Institute for Materials, State University of New York, Albany, New York 12203*

(Received 11 September 2001; accepted for publication 5 December 2001)

Ultrasonic-force microscopy (UFM) has been employed to carry out nanometer-scale mechanical imaging of integrated circuit (IC) test structures comprised of 0.32- $\mu\text{m}$ -wide aluminum interconnect lines inlaid in a low-dielectric-constant (low- $k$ ) polymer film. Such inlaid metal interconnects are typically referred to as damascene structures. UFM clearly differentiates the metal and polymer regions within this damascene IC test structure on the basis of elastic modulus with a spatial resolution  $\leq 10$  nm. In addition, this technique reveals an increase in the polymer elastic modulus at the metal/polymer interface. This nanometer-scale hardening corresponds to compositional modification of the polymer from the reactive ion etch (RIE) process used to form trenches in the polymer film prior to metal deposition. The reported direct, nondestructive nanometer-scale mechanical imaging of RIE-process-induced modifications of low- $k$  polymers in IC test structures offers expanded opportunities for mechanical metrology and reliability evaluation of such materials. © 2002 American Institute of Physics. [DOI: 10.1063/1.1447330]

## INTRODUCTION

Until recently, the performance of complementary metal–oxide–semiconductor integrated circuits (ICs) has been driven by the length scale of the transistor. Reductions in transistor gate length have led to increased transistor switching speed. However, this downward scaling of the gate length increases the density of metal lines used for transistor interconnects which, in turn, increases interline capacitive coupling ( $C$ ) and average interconnect resistance ( $R$ ). As the interconnect spacing moves below 0.13  $\mu\text{m}$ , the  $RC$  latency of the interconnect lines has emerged as a primary IC performance driver.<sup>1</sup> This has hastened the replacement of aluminum and  $\text{SiO}_2$  as the interconnect metal and insulator of choice for silicon-based ICs with copper and so-called low- $k$  dielectric materials to reduce the effective  $RC$  constant of the circuit.<sup>1</sup> Materials possessing low-dielectric constants that are chemically compatible with IC processing are typically organic polymers or porous silicates.<sup>2,3</sup> The former materials possess inherently low molecular polarizability, while the latter exhibit low mass density. One of the greatest challenges in incorporating these materials into microelectronic devices concerns the mechanical properties (bulk modulus, shear modulus, and Poisson's ratio) of these materials, which are typically far inferior to  $\text{SiO}_2$ . For example, several porous silicates ( $k \sim 2.2$ ) being considered as candidate low- $k$  materials possess Young's moduli as low as 2.5 GPa (compared to

$\sim 78$  GPa for  $\text{SiO}_2$ ).<sup>4</sup> Promising organic low- $k$  thermoset polymers, such as Dow Chemical's SiLK®, possess similar moduli in the range 2.7–3.0 GPa.<sup>5</sup>

The need for such materials will only increase in the near future. For the so-called 100 nm IC device node the 2000 International Technology Roadmap for Semiconductors calls for a dielectric constant for interlevel dielectrics between 1.6 and 2.2.<sup>1</sup> But, the degraded elastic performance of low- $k$  materials compared to  $\text{SiO}_2$  raises the risk of mechanical failure within the interconnect structure due to externally applied stresses in interconnect planarization processing, and/or due to thermally induced internal stresses from the thermal-expansion coefficient mismatch of the dielectric and metallic components. To effectively integrate low- $k$  materials in IC devices within these constraints, it is necessary to develop corresponding analytical and metrology techniques to directly image the mechanical properties of IC interconnect structures at the nanometer length scale. In this manner, the fundamental material properties governing stress-induced defect generation in nanometer-scale device structures can be directly investigated. In addition, so-called nanometer-scale mechanical imaging can be used as a unique tool for materials development for ICs and emerging nanotechnologies.<sup>6</sup>

In this article, we report the application of ultrasonic-force microscopy (UFM) to the nanometer-scale mechanical imaging of low- $k$  interconnect structures; namely, single-level damascene Al/divinylsiloxane-bis-benzocyclobutene (BCB) IC test structures. The observed image contrast from UFM scans of these test structures scaled with sample mechanical rigidity, clearly differentiating metal and dielectric regions. The UFM mechanical image contrast was also inde-

<sup>a)</sup>Electronic mail: rgeer@uamail.albany.edu

<sup>b)</sup>Present address: Symyx Technologies Inc., 3100 Central Expressway, Santa Clara, CA 95051.

pendent of surface topography that was measured (simultaneously) with standard atomic-force microscopy (AFM). Detailed mechanical imaging of metal/dielectric trench regions ( $0.32\text{ }\mu\text{m}$  feature size) also revealed an increase in the BCB polymer rigidity at the Al interface. Spectroscopic studies of this interface reveal a modification of the polymer composition due to the reactive ion etch (RIE) process used to form trenches in the polymer film prior to metal deposition. Specifically, the exposure of the BCB polymer surface regions to this RIE plasma promotes surface silicon-oxide formation in agreement with prior studies, enhancing the surface elastic modulus of the polymer as determined directly by UFM. The ability to nondestructively image such process-induced mechanical material modifications in an IC test structure demonstrates the utility of UFM in the future development of IC metrology techniques.

### EXPERIMENT: UFM CONFIGURATION AND OPERATION

Mechanical (UFM) and topography (AFM) image scans were acquired using ultrasonic-force microscopes configured from commercial AFM systems (Model CP, Park Scientific Instruments, and Digital Instruments Dimension 3100) employing SiN cantilever contact tips. The experimental configuration was similar to that reported by Dinelli *et al.*<sup>7</sup> In UFM imaging mode an ultrasonic vibration ( $f=2.2\text{ MHz}$ ) is applied to the sample in contact with an AFM probe tip. The ultrasonic frequency is far above the fundamental resonance of the cantilever resulting in inertial damping of the tip oscillation amplitude at the driving frequency. The effectively immobile SiN tip then periodically deforms the sample surface.<sup>8</sup> Appropriate modulation of the ultrasonic wave form exploits a nonlinearity in the tip-sample force-displacement curve. At a threshold ultrasonic oscillation amplitude the tip-sample force varies nonlinearly with the tip-sample relative displacement and results in a dc or low-frequency deflection of the AFM cantilever. This deflection can be related directly to the mechanical interaction between the tip and the sample.<sup>8</sup> The dc deflection wave form is recorded with a Tektronix TDS 220 digital oscilloscope and a lock-in amplifier (SRS 830), which passes the low-frequency deflection signal to the AFM imaging electronics. A standard raster from conventional scanning-probe software provides a sample contrast image related to the UFM threshold oscillation amplitude. Neglecting adhesive interactions, this image contrast increases monotonically with the local sample contact stiffness.<sup>9</sup>

Detailed investigations of the UFM imaging mode have been published on a wide array of material systems.<sup>6–10</sup> Differential elastic sensitivity in UFM imaging has been estimated at 0.08% for compound semiconductor materials, and in-plane (surface) spatial resolution of UFM has been estimated at better than 4 nm for certain material systems.<sup>9</sup> It is important to note that UFM in-plane spatial resolution is sensitive to surface topography, the presence of which can introduce artifacts in mechanical contrast through variations in the tip-sample contact area as a function of tip position. Fortunately, the simultaneous acquisition of UFM and AFM image data permits a direct point-by-point comparison of

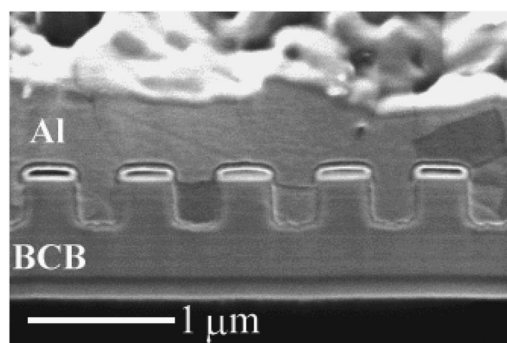


FIG. 1. FIB-SEM cross section of  $0.32\text{-}\mu\text{m}$ -wide trenches in a BCB matrix filled with CVD aluminum. The bright features at the top of the BCB trench walls correspond to  $\text{SiO}_2$  layers (hardmask) used as RIE resist layers. Note the complete Al fill of the trenches. Slight variations in Al contrast within the trenches correspond to different crystallographic orientations of the Al grains.

mechanical and topographic contrast for image artifact identification if severe surface topography is present. Estimates of UFM depth resolution are not nearly as complete as those for in-plane spatial resolution. Although Dinelli *et al.* have qualitatively modeled UFM tip-sample responses utilizing analytical models of the tip-sample elastic and adhesive interactions, quantitative and depth-dependent modeling of UFM contrast is still awaiting accurate models of nanoscale contact dynamics which have yet to be developed.<sup>7</sup> Still, observation of subsurface mechanical features have been reported in highly oriented pyrolytic graphite and, more recently, in nanoporous silicates.<sup>11–13</sup> An empirical determination of the depth sensitivity of UFM was recently completed by Geisler *et al.*<sup>14</sup> In those studies, it was demonstrated that UFM depth sensitivity to large, subsurface voids in crystalline Si extended to approximately 200 nm.

### EXPERIMENT: Al/BCB DAMASCENE TEST STRUCTURE FABRICATION

Single-level damascene IC test structures were used to evaluate mechanical nanoscale imaging via UFM. These consisted of thermal chemical-vapor deposited (CVD) aluminum in a RIE-patterned BCB matrix. The term damascene refers to an IC interconnect formation process whereby a series of trenches and holes are patterned into a blanket dielectric film. The patterned dielectric film is then coated with a thin ( $\sim 25\text{--}40\text{ nm}$ ) diffusion barrier layer followed by metal (in this case, CVD Al) deposition to completely fill the trenches and holes. After the excess metal is polished away by chemical-mechanical planarization (CMP), the filled trenches and holes comprise metal interconnect lines and vias.<sup>15</sup> For the structures studied here, a LAM 4520XL etching chamber was used to etch trench and via structures in films of BCB dielectric using an Ar (500 sccm),  $\text{O}_2$  (90 sccm), and  $\text{CF}_4$  (10 sccm) etchant gas flow mixture.<sup>16</sup> Diffusion barriers consisted of a bilayer stack of physical-vapor deposited (PVD)/CVD TiN. Aluminum CVD was employed to fill the metal lines. An FEI FIB-200 focused-ion-beam (FIB) scanning electron microscope (SEM) was used to obtain cross-section micrographs of CVD Al-filled trenches in BCB (shown in Fig. 1). Complete trench fill is evident. Fol-

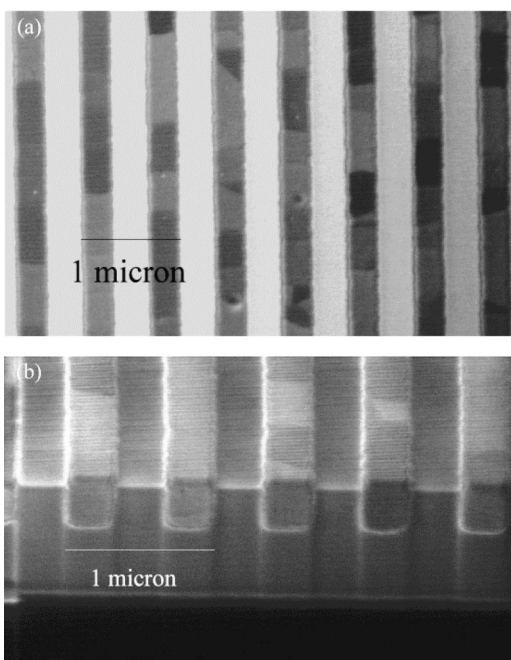


FIG. 2. Plan-view (a) and cross-sectional view (b) FIB-SEM micrographs of 0.32- $\mu\text{m}$ -wide, Al-filled trenches in a BCB matrix following chemical-mechanical planarization (CMP). In (a) the Al lines possess a darker contrast compared to the BCB trench walls. Variation in contrast within the Al lines correspond to different crystallographic orientations of Al grains. In the cross-section micrograph (b) the BCB trench walls appear depressed relative to the tops of the Al lines. This results from ablation of the BCB by Ga ions during ion milling and imaging in the FIB SEM. In actuality, the BCB trench walls extend above the tops of the Al lines following CMP.

lowing Al CVD, CMP was undertaken with a  $\text{HNO}_3$ -based slurry to remove the excess Al above the BCB trench walls.<sup>16</sup> Planarization yielded a single-level Al/TiN/BCB damascene interconnect structure. Plan-view and cross-sectional FIB micrographs of planarized Al trenches in BCB are shown in Figs. 2(a) and 2(b), respectively. The apparent depression of the BCB trench walls relative to the top of the Al lines in Fig. 2(b) is due to BCB ablation by Ga ions during FIB imaging. AFM studies of these structures prior to FIB imaging have shown the BCB trenches slightly elevated with respect to the tops of the Al lines following CMP.<sup>16</sup> This result is confirmed in AFM topographic data presented below.

This particular Al/BCB IC test structure was chosen for initial investigations of nanometer-scale mechanical imaging for several reasons. First, the elastic modulus contrast between Al (70 GPa) and BCB (4 GPa) is well suited to UFM. Second, the recent introduction of Cu interconnects in IC fabrication ensures that damascene processing will be the method of choice for the next several device generations and, hence, the most relevant for proof-of-concept testing of recently developed analytical or metrology techniques.<sup>1,15</sup> In addition, the performance of these particular Al/BCB damascene interconnect structures has been validated through thermal and electrical testing and provide a realistic example of a low- $k$ /metal interconnect structure encountered in IC fabrication.<sup>16</sup> Emerging Cu/low- $k$  interconnect structures will offer greater mechanical contrast due to the increased modulus of Cu (110 GPa) and reduced modulus of porous organic

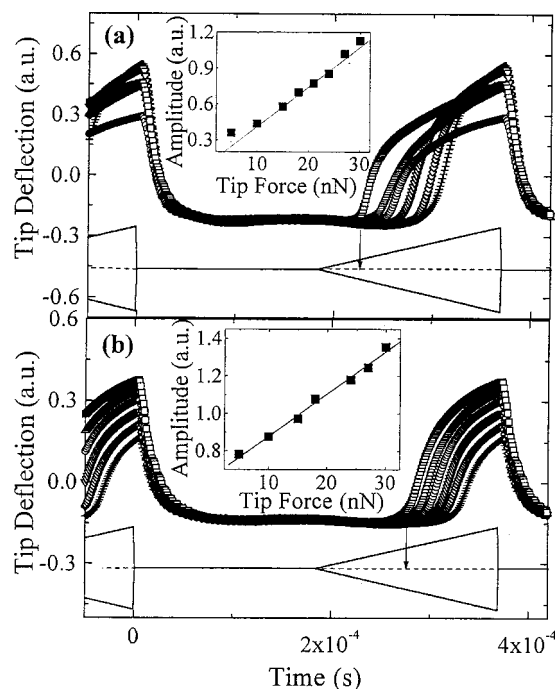


FIG. 3. Force-response curves taken from 20 nm $\times$ 20 nm UFM scans of (a) Al and (b) BCB sections of the test structure. The open symbols represent average tip deflection as a function of piezoelectric oscillation amplitude. The modulating wave form of the ultrasonic oscillation is shown at the base of the figure. Force-response curves corresponding to static tip forces of 10 nN (open squares), 15 nN (open triangles), 18 nN (open circles), 24 nN (inverted open triangles), 27 nN (open diamonds), and 30 nN (crosses) are shown. The threshold amplitude is defined by the sharp rise in the tip deflection (denoted by a small arrow for the 10 nN curves). The difference in the Al and BCB threshold amplitudes for the 10 nN static tip force reflects the difference in elastic constants between the two materials. The variations of threshold amplitude with applied tip force are shown in the respective insets.

polymers and high-porosity dielectrics ( $<2$  GPa).<sup>4,5</sup>

Compositional analyses of BCB and TiN films were carried out by x-ray photoelectron spectroscopy (XPS). XPS studies were carried out with a Perkin-Elmer PHI 550 XPS system. The source for XPS photons was a dual-anode x-ray source at 15 kV and 300 W. The anode used was magnesium with a characteristic energy of 1253.6 eV with a full width at half maximum of 0.7 eV. XPS depth profiling utilized an Ar-ion sputter beam. On insulating substrates care was taken to minimize charging effects.

## RESULTS AND DISCUSSION

Prior to topographic and elastic imaging of Al/BCB interconnect structures, UFM tip-deflection curves were recorded from separate 20 nm $\times$ 20 nm scans on isolated Al and BCB regions to confirm the nonlinear rectification of the ultrasonic oscillation. These data, captured from a digital oscilloscope, are shown in Figs. 3(a) and 3(b), respectively. The triangular ultrasonic vibration modulation wave form applied to the Al/BCB sample is shown in the bottom of each plot as a function of time. The various symbol data reflect the AFM differential photodiode signal response (i.e., tip deflection) to the modulated ultrasonic wave form for applied static tip forces ranging from 10 to 30 nN (see Fig. 3 caption).



Kolosov and co-workers noted that no tip deflection would result from a modulated ultrasonic sample vibration if the tip-sample force-deflection curve were linear.<sup>8</sup> Instead, the rapid onset of the tip-deflection signal in the photodiode response data of Fig. 3 denotes a nonlinearity in the tip-sample interaction due, primarily, from variation in tip-surface force as a function of relative tip-sample displacement. The associated point on the modulation wave form defines a threshold vibration amplitude [denoted by arrows in Figs. 3(a) and 3(b) for an applied tip force of 10 nN]. This threshold amplitude should scale monotonically with applied tip force, as shown in the insets of Figs. 3(a) and 3(b), and confirms the UFM signal is directly related to the elastic modulus of the sample. Fixing the applied tip force, the subsequent variation in the critical vibration amplitude (and, hence, tip-deflection wave form) as the tip is scanned across the IC test structure results in a UFM image contrast primarily proportional to material elasticity. The lower mechanical response of the polymer compared to the aluminum is readily seen by the larger threshold amplitude required for tip deflection [Fig. 3(b)]. The individual tip-deflection wave forms for the polymer exhibit notable differences compared to the same curves for aluminum. These systematic variations are presumed to result from differences in the viscoelastic responses and adhesion interactions of the two materials to the ultrasonically impinging AFM tip.

Dinelli *et al.* have demonstrated that proper calibration of the threshold modulation amplitude as a function of applied tip force can be exploited to extract the contact stiffness and reduced Young's modulus.<sup>7</sup> To do so with high precision and accuracy requires the local sample surface vibration amplitude and detailed knowledge of the tip-surface contact area. Applications of such methods to the structures studied here are currently underway.

Large length-scale topography (AFM) and mechanical (UFM) images of the Al/BCB test structure are shown in Fig. 4. This  $40\text{ }\mu\text{m} \times 40\text{ }\mu\text{m}$  scan images an Al trench field ( $0.32\text{ }\mu\text{m}$  trench width) adjacent to a chessboard contact pad. Note the  $10\text{-}\mu\text{m}$ -wide Al lead atop the trench field. The surface topography of the metal/low- $k$  surfaces shown in Fig. 4(a) is indicative of height variations expected from CMP processing of Al/BCB test structures.<sup>16</sup> Aluminum removal rates via CMP increase with Al fill factor resulting in depressions of the large Al lead and contact pad areas in comparison with the Al trench region. The CMP process utilized here exhibited a higher Al removal rate compared to that of BCB, resulting in the elevation of BCB trench walls and fields relative to Al, also evident in Fig. 4(a). In sharp contrast, the UFM image of Fig. 4(b) displays no topographical sensitivity. The UFM image contrast is material specific, clearly delineating polymer and Al regions uniformly across the scan area. The image contrast corresponding to Al is uniform across the trench region, the  $10\text{-}\mu\text{m}$ -wide lead, and the contact pad. The majority of the BCB area also possesses the same relative UFM contrast, with the exception of isolated dark lines between the contact pad and trench field that are attributed to scanning artifacts.

The image data of Fig. 4 data clearly illustrates the elastic differentiation capability of UFM mechanical imaging

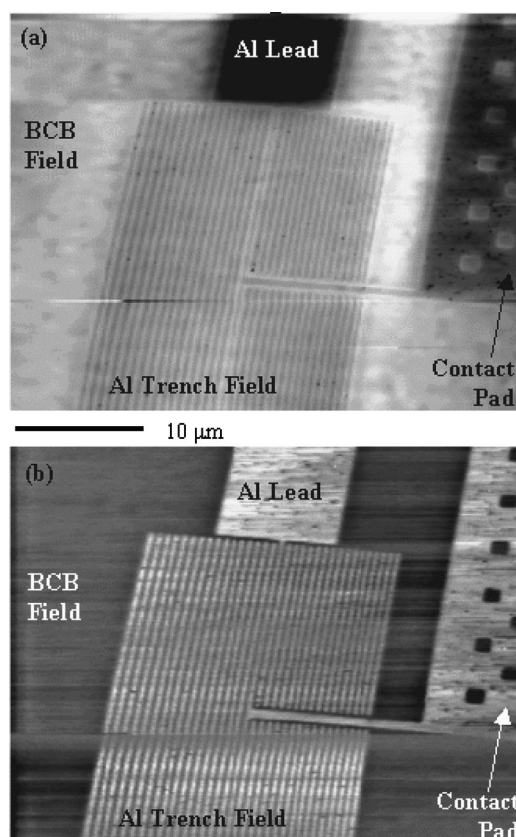


FIG. 4.  $40\text{ }\mu\text{m} \times 40\text{ }\mu\text{m}$  AFM (a) and UFM (b) image scans across a trench/lead area in the Al/BCB test structure (reprinted from Ref. 6). A field consisting of  $0.32\text{-}\mu\text{m}$ -wide Al trenches, a  $10\text{-}\mu\text{m}$ -wide Al lead, and an Al/BCB chessboard contact pad are labeled. The topographic variations between these regions in the AFM image result primarily from the fill-factor dependence of the CMP removal rate. Contrary to this, the UFM contrast is sensitive only to the relative elastic modulus of the materials, providing a nanometer-scale image of the mechanical properties of the structure.

with respect to metal interconnects in a low- $k$  dielectric matrix. Figure 5 displays higher-resolution topography and elastic images of the  $0.32\text{ }\mu\text{m}$  Al trench region. The topographic image contrast of Fig. 5(a) results from the disparity between Al and BCB CMP removal rates (as noted above), while the mechanical image contrast of Fig. 5(b) results primarily from the difference between the Al and BCB elastic moduli in agreement with the threshold ultrasonic vibration amplitudes shown in Fig. 3. Unambiguous material identification of these features was confirmed by comparing topographic and elastic signatures with the nearby BCB field. Closer analysis of Fig. 5(a) yields an average Al linewidth of  $0.32 \pm 0.010\text{ }\mu\text{m}$  and an average BCB trench wall width approximately 10% larger. Both values are in agreement with previous studies as well as the FIB image data of Figs. 1 and 2.<sup>16</sup> Except in the immediate vicinity of isolated contaminants, the UFM mechanical response in Fig. 5(b) is uniform across the Al lines. However, there is no feature readily identifiable with the TiN liner layer between the Al and the BCB regions, estimated at 35 nm from FIB cross sections.<sup>16</sup> This layer would be expected to have a larger contact stiffness compared to the Al line, assuming the TiN barrier possessed a bulk-like modulus of 251 GPa. This assumption is questionable, as *in situ* quantitative modulus measurements on TiN

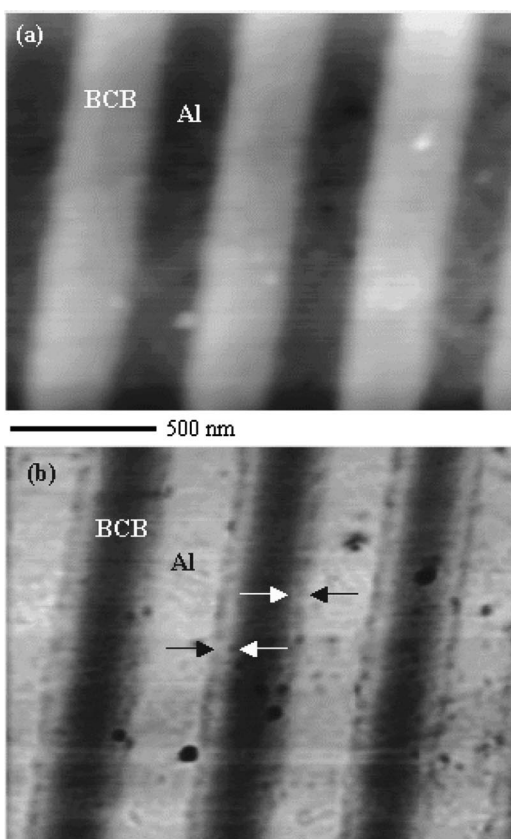


FIG. 5. AFM (a) and UFM (b) scans in the trench region of the Al/BCB damascene test structure imaged in Fig. 4 (reprinted from Ref. 6). Note the inversion of the contrast between topography (a) and elasticity (b) scans. Note the interfacial variation of the elasticity between the Al and BCB regions. The Al/BCB interface is denoted at two points in the image by black arrows. The interface of the hardened BCB and unmodified BCB is denoted at two points in the image by white arrows. The AFM/UFM images were acquired via bidirectional horizontal (relative to the figure) scans of the probe tip.

barrier films have not been reported and CVD films often possess reduced mass density and elastic moduli compared to accepted bulk values. For example, Young's moduli measured from CVD  $\text{Si}_3\text{N}_4$  films vary from 112 to 300 GPa depending upon process parameters.<sup>17</sup> Oxidation and concomitant hardening of the Al surfaces during and after CMP may also obscure the elastic contrast between the Al/TiN regions. Detailed understanding of the depth dependence of the UFM response is required to fully address this possibility. The presumed position of the TiN barrier layer also corresponds to a significant change in the topography, as seen in Fig. 5(a). The average height differential between the Al and BCB regions varies between 3 and 4 nm (see above). The lateral topographic width of this interface (without tip deconvolution) is approximately 50 nm, yielding a minimum feature inclination of approximately  $4^\circ$ . Topography variations on this scale are not usually problematic with respect to UFM imaging and would not be expected to obscure variations in surface elastic response occurring on length scales significantly exceeding 10 nm.

A striking feature of Fig. 5(b) is the mechanical nonuniformity across the top of the BCB trench wall. Two distinct regions are evident. The center portion of the BCB trench

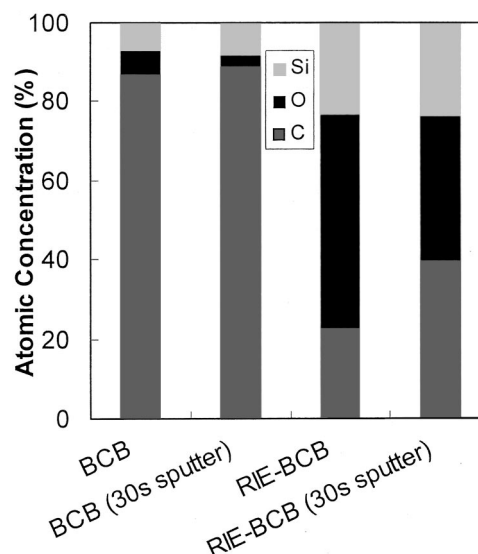


FIG. 6. Elemental composition of non-RIE-exposed and RIE-exposed BCB blanket polymer films via XPS (reprinted from Ref. 6). One set of data corresponds to standard surface XPS. The second set of data was acquired following a 30 s *in situ* Ar-ion sputter. The atomic composition of the as-received BCB films is as expected. Note, however, the dramatic reduction in carbon concentration and relative increase in Si and O concentrations for the RIE-exposed BCB film. A similar atomic composition remains after 30 s of sputtering indicating a strong depth dependence of the effects of RIE exposure.

wall displays a lower contact stiffness compared to high-contrast regions near the Al/BCB interfaces. It is important to note that these interfacial regions are *within* the BCB trench wall as confirmed by topographic and FIB cross-section data. These areas do not correspond to the TiN liner. The interfacial regions of the BCB trench wall vary in width between  $75 \pm 10$  and  $110 \pm 10$  nm from the data in Fig. 5(b). If it is assumed the UFM tip/sample interaction is dominated by the surface elastic response, this gradation in the mechanical image contrast indicates a rapid increase in BCB rigidity as the Al/BCB interface is approached. Spectroscopic studies were undertaken on blanket films of RIE-exposed BCB to ascertain possible process-induced compositional variations responsible for such mechanical variations seen in the data of Fig. 5. Figure 6 compares atomic composition measured via x-ray photoelectron spectroscopy between an as-deposited BCB blanket film and a BCB blanket film exposed to the RIE plasma.<sup>16,18</sup> The surface of the RIE-exposed BCB film is oxygen rich and carbon deficient, resulting in a silicon-oxide-rich surface. More significant is that this composition extends well into the BCB, as shown by composition measurements made following a 30 s Ar-ion sputter (also shown in Fig. 6). It is estimated that this 30 s sputter removes approximately 30 nm of BCB polymer.<sup>19</sup> These data are consistent with recent work by Vitale, Chae, and Sawin, where the use of  $\text{O}_2$  RIE plasmas completely converted the surface of BCB films to silicon dioxide.<sup>20</sup> Although that work did not estimate the depth dependence of the plasma-induced compositional modification of the BCB, the lack of a carbon signal from *in situ* surface XPS measurements carried out after  $\text{O}_2$  plasma etching implies a lower-bound estimate of 6 nm.<sup>21</sup>

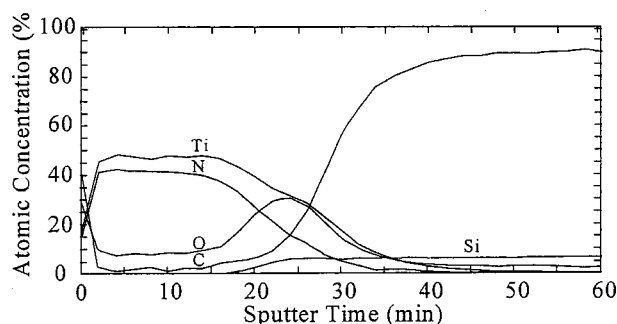


FIG. 7. Elemental composition depth profile of a PVD TiN/RIE-exposed BCB blanket bilayer film from XPS (reprinted from Ref. 6). Note the maximum in oxygen concentration as the TiN/BCB interface is approached. In addition, the relative carbon concentration at this interface is well below the value expected for unmodified BCB while the Si concentration quickly reaches the level found in the bulk BCB. This supports the observation of an elastic modulus modification of the BCB in the vicinity of the RIE-exposed surface.

These RIE-induced compositional modifications will subsequently alter the BCB surface mechanical response. Prior to drawing conclusions, however, it is also necessary to examine the effect of TiN barrier deposition on RIE-exposed BCB to determine if the presence of the TiN film significantly altered the composition profile of the etched BCB. Figure 7 displays XPS depth profiling of RIE-exposed BCB stacks coated with a PVD TiN film.<sup>16</sup> Consistent with the data in Fig. 6, the oxygen concentration exhibits a pronounced peak at the TiN/BCB interface. The Si atomic concentration saturates within this interfacial region while the carbon concentration does not rise to the BCB bulk value until well below the TiN/BCB interface. Similar compositional profiles from TiN layers deposited on untreated BCB films lack this RIE-induced oxygen peak.<sup>22</sup> These data confirm the presence of a silicon-oxide-rich region at the TiN/BCB interface and provide a compositional explanation for the mechanical image contrast variation seen in Fig. 5; specifically, the interfacial rigidity of the BCB dielectric is dramatically enhanced as a result of local silicon-oxide formation resulting from the RIE process. More importantly, from a characterization and mechanical metrology point of view, this mechanical modification extends a significant distance ( $>75$  nm) into the BCB trench wall.

The impact of this demonstration on future IC metrology is noteworthy. Metal/low- $k$  IC interconnect structures are particularly susceptible to thermal stresses encountered in wire bonding, packaging, and normal operation.<sup>5</sup> Consequently, optimizing thermal and mechanical performance requires precise spatial determination of mechanical modulus for accurate mechanical software simulators to be used effectively. Nanometer-scale mechanical imaging via UFM provides a nondestructive, direct technique to extract these data, instead of relying on indirect measurements from blanket low- $k$  dielectric films or blanket low- $k$  dielectric/metal multilayer stacks. A second and perhaps more vital capability of UFM is direct imaging of nanoscale mechanical defects in damascene metal/low- $k$  dielectric structures. The work presented here confirms that the spatial resolution and mechanical contrast of UFM may be suitable for such applications.

Preliminary efforts of applying UFM in this area show extremely high promise and will be reported elsewhere.

## CONCLUSIONS

A characterization technique based on ultrasonic-force microscopy has been demonstrated with the capability of imaging the nanometer-scale mechanical properties of Al/low- $k$  damascene IC test structures. Using UFM imaging, it was possible to differentiate the metal and dielectric regions of this test structure on the basis of elastic modulus with a spatial resolution  $\leq 10$  nm. Moreover, this technique has revealed process-induced mechanical variations of the low- $k$  dielectric polymer within the test structure itself, opening expanded opportunities for metrological evaluation of process-dependent mechanical properties of low- $k$  dielectrics and associated optimization of low- $k$  integration processes for IC fabrication.

## ACKNOWLEDGMENTS

The authors gratefully acknowledge J. Hummel and J. Liu for BCB test structure patterning/CMP, and support from the Dow Chemical Company, the Microelectronics Advanced Research Corporation, and the New York State Center for Advanced Thin Film Technology.

- <sup>1</sup>The International Technology Roadmap for Semiconductors (Semiconductor Industry Association, San Jose, CA, 2000).
- <sup>2</sup>C. H. Ting, T. E. Seidel, Mater. Res. Soc. Symp. Proc. **381**, 3 (1995).
- <sup>3</sup>L. W. Hrubesh, Mater. Res. Soc. Symp. Proc. **381**, 267 (1995).
- <sup>4</sup>C. Jin and J. Wetzell, Proceedings of the International Interconnect Technology Conference (2000), pp. 99–101 (unpublished).
- <sup>5</sup>R. D. Goldblatt, B. Agarwala, M. B. Anand, E. P. Barth, G. A. Biery, Z. G. Chen, S. Cohen, J. B. Connolly, A. Cowley, T. Dalton, S. K. Das, C. R. Davis, A. Deutsch, C. DeWan, D. C. Edelstein, P. A. Emmi, C. G. Faltermeyer, J. A. Fitzsimmons, J. Hedrick, J. E. Heidenreich, C. K. Hu, J. P. Hummel, P. Jones, E. Kaltalioglu, B. E. Kastenmeier, M. Krishnan, W. F. Landers, E. Liniger, J. Liu, N. E. Lustig, S. Malhotra, D. K. Manger, V. McGahay, R. Mih, H. A. Nye, S. Purushothaman, H. A. Rathore, S. C. Seo, T. M. Shaw, A. H. Simon, T. A. Spooner, M. Stetter, R. A. Wachnik, and J. G. Ryan, Proceedings of the International Interconnect Technology Conference (2000), pp. 261–263 (unpublished).
- <sup>6</sup>G. S. Shekhawat, O. V. Kolosov, G. A. D. Briggs, E. O. Shaffer, S. J. Martin, and R. E. Geer, Proceedings of the International Interconnect Technology Conference (2000), pp. 96–98 (unpublished).
- <sup>7</sup>F. Dinelli, S. K. Biswas, G. A. D. Briggs, and O. V. Kolosov, Phys. Rev. B **61**, 13995 (2000).
- <sup>8</sup>O. V. Kolosov and K. Yamanaka, Jpn. J. Appl. Phys., Part 1 **32**, 1095 (1993).
- <sup>9</sup>F. Dinelli, M. R. Castell, D. A. Ritchies, N. J. Mason, G. A. D. Briggs, and O. V. Kolosov, Philos. Mag. A **80**, 2299 (2000).
- <sup>10</sup>O. V. Kolosov, M. R. Castell, C. D. Marsh, G. A. D. Briggs, T. I. Kamins, and R. S. Williams, Phys. Rev. Lett. **81**, 1046 (1998).
- <sup>11</sup>K. Yamanaka, MRS Bull. **21**, 36 (1996).
- <sup>12</sup>K. Yamanaka, H. Ogiso, and O. Kolosov, Appl. Phys. Lett. **64**, 178 (1994).
- <sup>13</sup>R. E. Geer and G. S. Shekhawat, (unpublished results).
- <sup>14</sup>H. Geisler, M. Hoehn, M. Rambach, M. A. Meyer, E. Zschech, M. Mertig, A. Romanov, M. Bobeth, W. Pompe, and R. E. Geer, Proceedings of the XIIth International Conference on Microscopy of Semiconducting Materials (2001) (unpublished).
- <sup>15</sup>P. Van Zant, *Microchip Fabrication: A Practical Guide to Semiconductor Manufacturing* (McGraw-Hill, New York, 1997), pp. 502–514.
- <sup>16</sup>H. Gundlach, R. Talevi, Z. Bian, G. Nuesca, S. Sankaran, K. Kumar, A. E. Kaloyeros, R. E. Geer, J. Liu, J. Hummel, E. O. Shaffer, and S. J. Martin, J. Vac. Sci. Technol. B **18**, 2463 (2000).
- <sup>17</sup>T. Cramer and O. Paul, Sens. Actuators A **92**, 292 (2001).
- <sup>18</sup>R. Talevi, H. Gundlach, Z. Bian, A. Knorr, M. van Gestel, S. Padiyar, A.

- E. Kaloyeros, R. E. Geer, E. O. Shaffer, and S. Martin, J. Vac. Sci. Technol. B **18**, 252 (2000).
- <sup>19</sup>The estimated sputtering of BCB by the Ar-ion beam (30 s exposure) in the XPS chamber was mistakenly reported in Ref. 15 as 5 nm. That value was for aluminum. The correct estimate for BCB is approximately 30 nm as determined by profilometry.
- <sup>20</sup>S. A. Vitale, H. Chae, and H. H. Sawin, J. Vac. Sci. Technol. A **18**, 2770 (2000).
- <sup>21</sup>T. L. Barr, *Modern ESCA: The Principles and Practice of X-Ray Photoelectron Spectroscopy* (CRC, Boca Raton, FL, 1994), p. 74.
- <sup>22</sup>R. Talevi, Ph.D. thesis, University at Albany, State University of New York (2000).